Electronic Supplementary Material (ESI) for Dalton Transactions.
This journal is © The Royal Society of Chemistry 2021

Supporting Information

New organometallic ruthenium(II) complexes with purine analogs - a wide perspective on their biological application

Marzena Fandzloch,*[a] Tomasz Jędrzejewski, [b] Liliana Dobrzańska, [c] Ginés M. Esteban-Parra, [d] Joanna Wiśniewska, [c] Agata Paneth, [e] Piotr Paneth [f] and Jerzy Sitkowski [g,h]

[a] Institute of Low Temperature and Structure Research, Polish Academy of Sciences, Okólna 2, 50-422 Wrocław, Poland.

[b] Department of Immunology, Faculty of Biological and Veterinary Sciences, Nicolaus Copernicus University in Toruń, Lwowska 1, 87-100 Toruń, Poland.

[c] Faculty of Chemistry, Nicolaus Copernicus University in Toruń, Gagarina 7, 87-100 Toruń, Poland.

[d] Department of Inorganic Chemistry, University of Granada, Avda. Severo Ochoa s/n, 18071 Granada, Spain.

[e] Department of Organic Chemistry, Faculty of Pharmacy, Medical University of Lublin, Chodźki 4a, 20-093 Lublin, Poland.

[f] Institute of Applied Radiation Chemistry, Faculty of Chemistry, Lodz University of Technology, Żeromskiego 116, 90-924 Lodz, Poland.

[g] National Institutes of Medicines, Chełmska 30/34, 00-725 Warszawa, Poland.

[h] Institute of Organic Chemistry, Polish Academy of Sciences, Kasprzaka 44/52, 01-224 Warszawa, Poland.

*Corresponding author e-mail:

m.fandzloch@intibs.pl

Table of Contents

Table S1…… 4

Fig. S1……... 5

Fig. S2……... 6

Molecular docking - validation……. 7

Fig. S3……... 8

Fig. S4……...…… 8

Quantum mechanical calculations…..……... 9

Table S2…… 9

Fig. S5……..……. 10

Fig. S6..... 10

Fig. S7..... 11

Fig. S8…….…….……. 11

Fig. S9…….…….……. 12

Fig. S10…….……..…..……. 12

Fig. S11…….……...……. 13

Fig. S12…….....……. 13

Fig. S13……. 14

Fig. S14……. 14

Fig. S15……. 15

Fig. S16……. 15

Fig. S17……. 16

Fig. S18……. 16

Fig. S19……. 17

Fig. S20……. 17

Fig. S21……. 18

Fig. S22……. 19

Fig. S23……. 19

Fig. S24……. 20

Fig. S25…….…… 21

Fig. S26…….…… 22

Fig. S27…….…… 23

Fig. S28…… 24
Fig. S29…… 25
Molecular packing……. 25
Fig. S30…… 26
Fig. S31…… 26
Fig. S32…… 27
Fig. S33…… 27
Fig. S34…… 28
Fig. S35……. 28
Fig. S36……. 29

Table S1. Data of lipophilicity details

complex	λ [cm^{-1}]	ε_λ [$M^{-1}cm^{-1}$]	log $P_{o/w}$ ± SD
1	405	75	0.05 ± 0.003
2	409	79	0.16 ±0.01
3	417	79	0.27 ± 0.01
NAMI-A	450	61	-2.31 ± 0.14

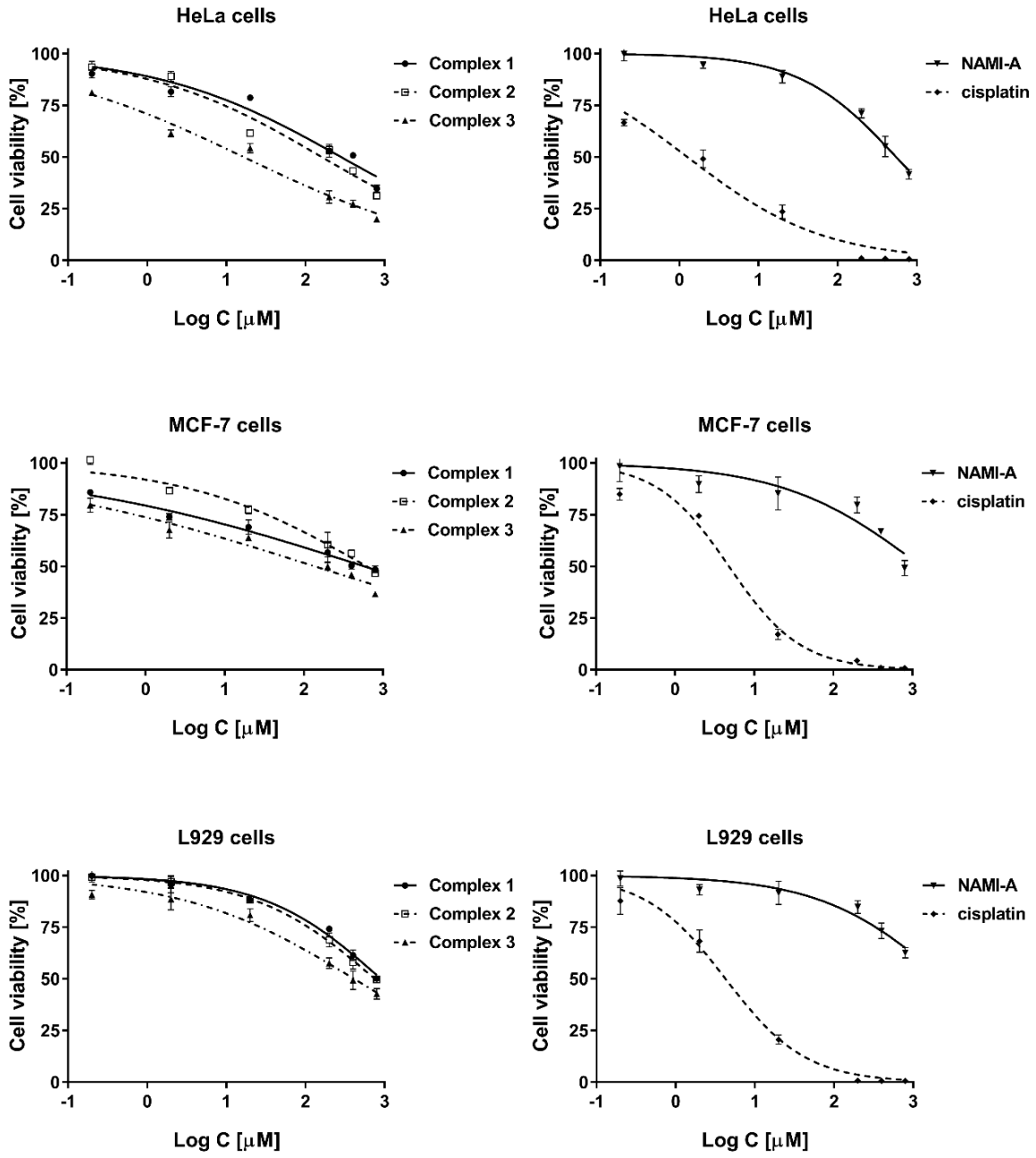

Fig. S1 The fit for the dose-response curves for data obtained during the MTT test.

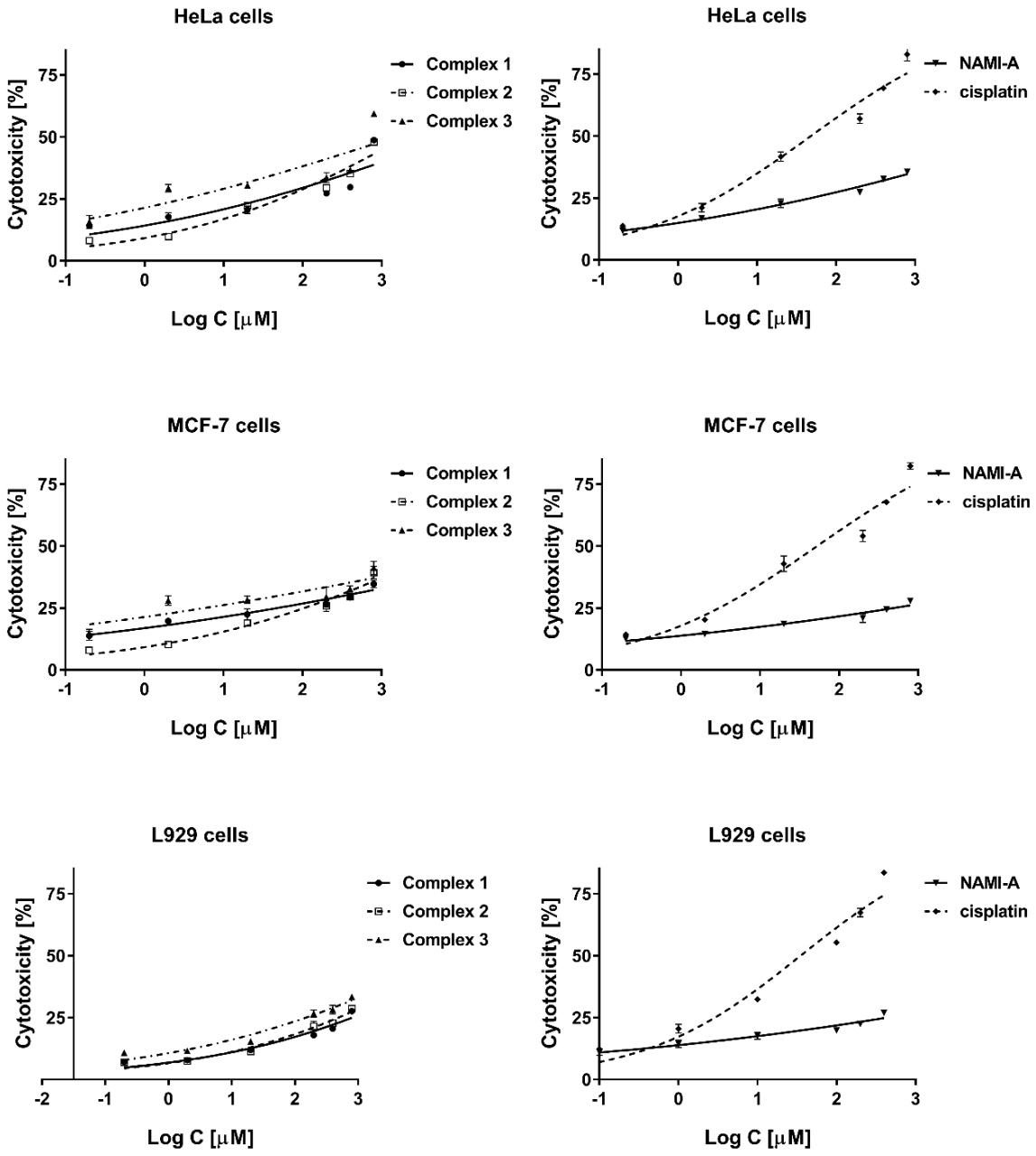

Fig. S2 The fit for the dose-response curves for data obtained during the LDH test.

Molecular docking

Validation. A few recent reports on studies of interactions of ruthenium complexes with proteins and DNA using molecular docking can be found in the literature.[1-6] Docking to DNA is a fairly new,[7,8] and unexplored area as the majority of docking programs were designed and tested for docking to proteins. Furthermore, the docking of metal complexes poses yet another problem. Since thus far no systematic evaluation of methodologies used for docking ruthenium complexes has been carried out, before starting our studies, we have decided to explore the capabilities of the software available to us and validate its performance by comparing with published results.

Within the six recently published relevant studies, five different docking programs have been used. The first two[1,2] employed the Autodock family of the programs; version 4.2[9] and Vina,[10] respectively. The problem with these programs is that out of metals, only iron has been included in the parameters optimization set. Parameters for ruthenium (and several other elements) were added to Autodock as an auxiliary, nonoptimized set. As far as we know, ruthenium parameters are not available in Vina. The next pair of publications[3,4] employed less popular nowadays docking tools implemented in Discover Studio (Cdocker)[11] and Sybyl[12] programs. In the last two Hex 6.1 docking program has been used.[13] Since this is the only case of two independent applications of a docking program for studies of ruthenium complexes we have decided to use it for our validation purpose. One of the approaches to dealing with atoms for which dependable parametrization does not exist is to use an analogous system for which such parameters have been created. In our case, we considered using iron complexes as proxies to those containing ruthenium. Thus initially we have optimized quantum-mechanically structures of the (η^6-*p*-$MeC_6H_4Pr^i$)RuCl(5-(4-methylthiophenyl)-dipyrromethene) complex, which was used in studies reported in reference 6 (complex **2**) and its iron analog (details on QM calculations are given below), and used these structures as ligands for docking to the same as the reported structure of human serum albumin (PDB[14] ID: 1H9Z[15]). With the root-mean-square (rms) deviation between these complexes of only 0.15 Å the structures are practically indistinguishable, as illustrated in Fig. S3. At our hands, the ruthenium complex occupies the same place as reported in the literature (compare Fig. S4a with Fig. 12 of reference 6) with major interactions to LYS195, TRP214, ARG218, and ASP451 (see Fig. S4b). Subsequently, the iron-containing complex has been docked. Three different levels of docking strategies available in Hex have been tested, with shape fit only, shape and electrostatic

interactions, and shape, electrostatics, and DARS[16] approach. At the first two levels of the docking accuracy, the best poses of ruthenium and iron complexes are indistinguishable, and only at the highest level negligible change in docking orientation (see Fig. S4c) has been observed. We took these results as confirmation that iron-containing analogs of the ruthenium complexes are good proxies for docking studies and we used them in the studies reported herein.

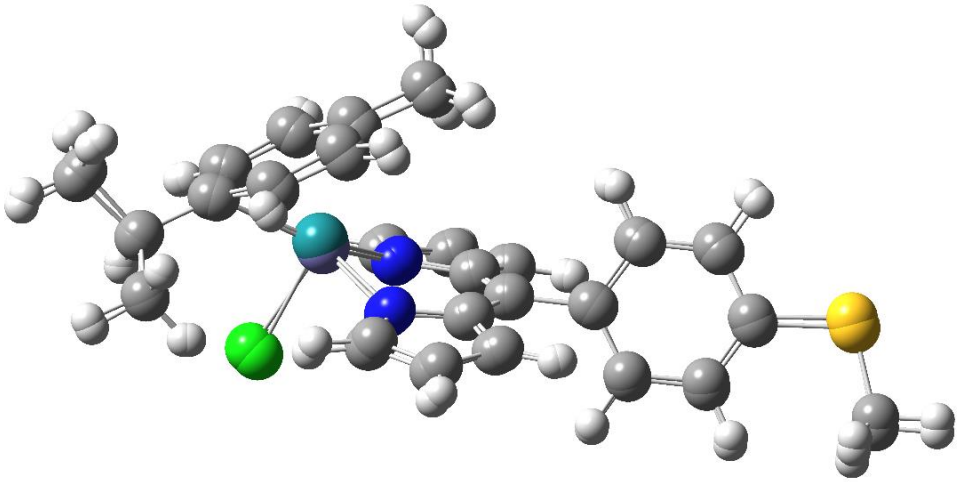

Fig. S3 The overlay of the rms fit of [(η^6-*p*-cym)Ru(detp)Cl_2] (**2**) with ruthenium substituted for iron. Both structures are optimized at the DFT level.

With iron analogs, we considered using Vina justified (singel Fe was included in the parametrization set). However, both Vina and Hex docking programs did not perform too well under conditions of blind docking. The sequence of clusters and the best poses exhibited quite widespread with small energy differences. We have, therefore, tested another popular docking program, Gold,[17] which was found to perform very well in the recent benchmark of docking programs,[18] as well as in our previous studies.[19]

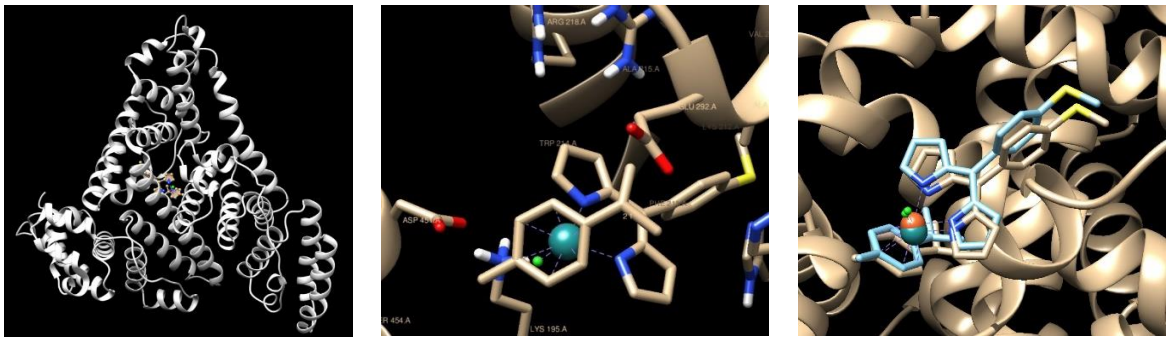

Fig. S4 (η^6-*p*-$MeC_6H_4Pr^i$)RuCl(5-(4-methylthiophenyl)-dipyrromethene) complex docked to HAS. View of the whole enzyme (a), details of interactions within the binding site (b), overlay of the docking poses (c).

Quantum mechanical calculations. Structures of the ruthenium and iron complexes have been optimized at the DFT level of theory using ωB97X-D functional[20,21] expressed in the def2-TZVP basis set[22] as implemented in the Gaussian16 program.[23] This theory level is becoming a new "golden standard" among practical theory levels for chemical calculations.[24] As can be seen from the results collected in Table S2 there is an excellent match between geometries obtained for ruthenium and iron complexes. Furthermore, the overlap with the experimental result from the X-ray is also very good. For example, the rms fit between the X-ray structure and the QM structure of ruthenium complex **1** is only 0.26 Å, and between the ruthenium complex and the iron complex, it is 0.08 Å. The overlap of these structures is illustrated in Fig. S5. Furthermore, both these complexes exhibit practically the same dipole moment; 12.03 D, and 12.15 D, respectively, indicating close electrostatic properties. These findings reinforce our approach of using iron complexes as proxies for ruthenium ones (in fact we have compared docking of complexes of these two metals in Gold and again found only negligible differences, however, we prefer discussing results for iron since ruthenium is not specifically parametrized in Gold and calculations default to generic parameters).

Table S2. Comparison of geometrical parameters of experimental and calculated complexes[a]

parameter	**2** (from ref. 6)		**1**			**2**		$\mathbf{3_{NH}}$[b]	$\mathbf{3_{OH}}$
	QM	QM-Fe	X-ray	QM	QM-Fe	X-ray	QM	QM	QM
M-Cl(1)	2.395	2.289	2.440	2.415	2.303	2.429	2.411	2.399	2.411
M-Cl(2)	-	-	2.432	2.411	2.305	2.421	2.414	2.400	2.414
M-N(1)	2.080	1.964	2.124	2.145	2.024	2.139	2.145	2.157	2.145
M-N(2)	2.072	1.953	-	-	-	-	-	-	-
$(M\text{-}C_{ar})_{min}$	2.162	2.147	2.176	2.154	2.147	2.176	2.154	2.156	2.154
$(M\text{-}C_{ar})_{max}$	2.218	2.225	2.205	2.203	2.219	2.224	2.203	2.211	2.203
$(M\text{-}C_{ar})_{ave}$	2.190	2.181	1.669	1.679	1.675	1.681	1.659	1.665	1.659
$M\text{-}C_{\omega}$	1.664	1.659	2.189	2.178	2.178	2.195	2.178	2.186	2.178
N(1)-M-Cl(1)	87.9	92.0	82.2	83.7	87.5	83.4	84.0	83.6	83.7
N(1)-M-Cl(2)	-	-	86.2	83.9	87.3	84.0	83.3	82.7	83.5
N(2)-M-Cl(2)	87.0	90.8	-	-	-	-	-	-	-
$N(1)\text{-}M\text{-}C_{ar\text{-}Me}$	113.4	111.6	118.4	121.9	119.9	123.3	121.7	122.4	121.9
$N(2)\text{-}M\text{-}C_{ar\text{-}Me}$	90.9	89.3	-	-	-	-	-	-	-

[a] M stands for the metal (Ru or Fe), subscripts min, max, and ave denote minimal, maximal, and the average distance between metal and carbon atoms (marked by subscript ar) of the aromatic ring of the η^6-*p*-$MeC_6H_4Pr^i$ substituent. Furthermore, subscript ω defined the point in the center of this aromatic ring, while ar-Me the carbon atom of the ring to which the methyl group is attached.

[b] $\mathbf{3_{NH}}$ corresponds to complex **3** containing the keto form and $\mathbf{3_{OH}}$ the enol form of HmtpO (Fig. S6).

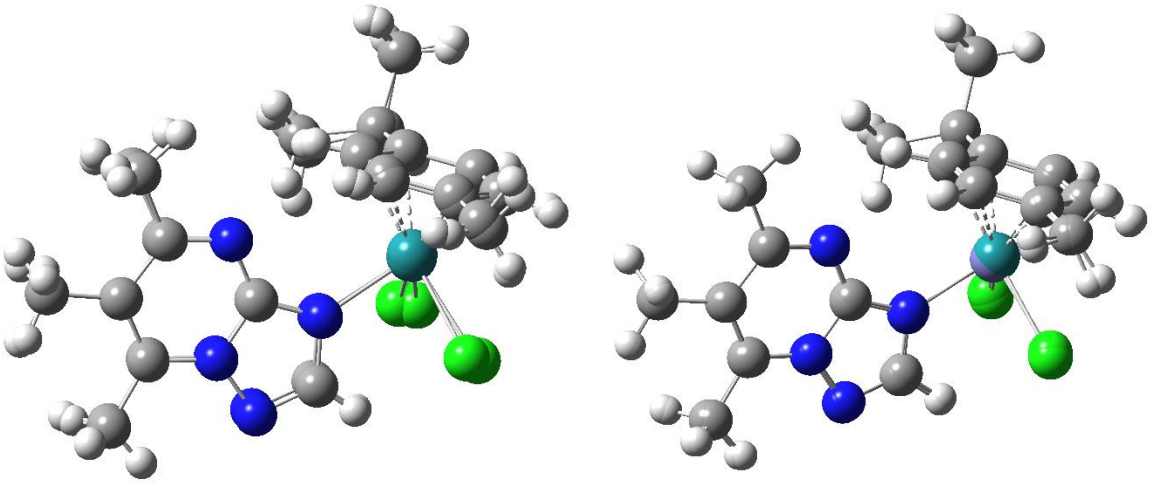

Fig. S5. Overlaps of different **1** structures. QM vs. X-ray (a); Fe vs Ru (b).

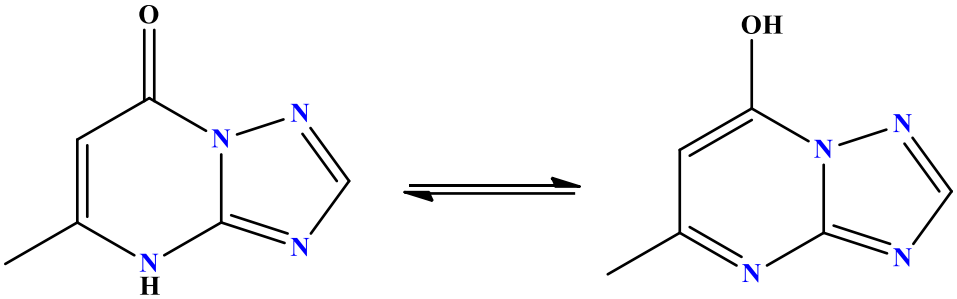

Fig. S6 The keto and enol forms of HmtpO.

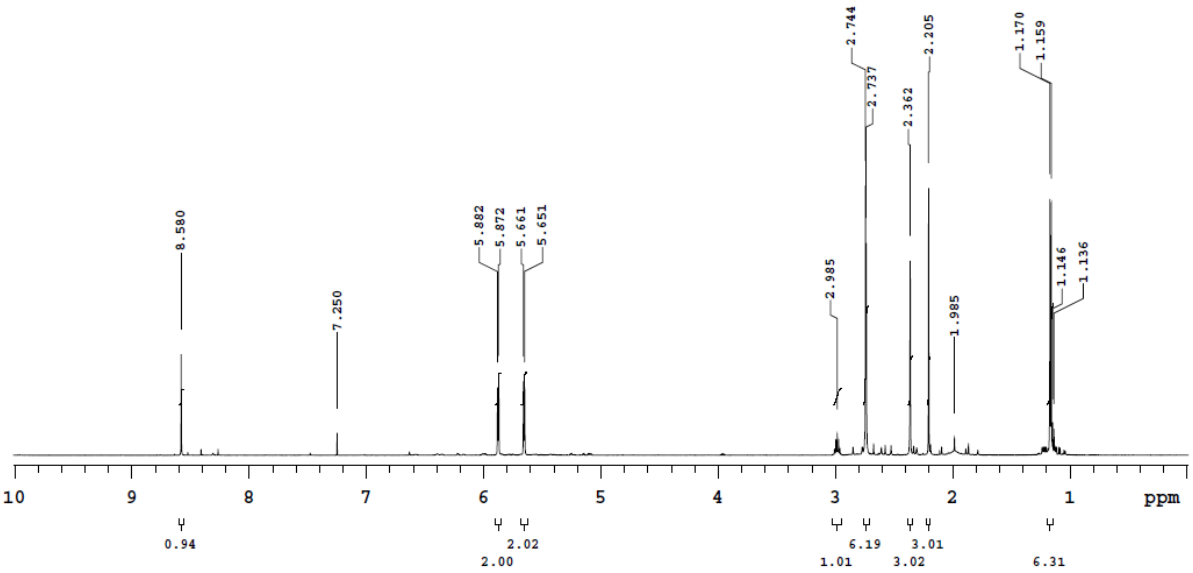

Fig. S7 ^{1}H NMR spectrum recorded for the [(η^6-*p*-cym)Ru(tmtp)Cl_2] (**1**) in $CDCl_3$.

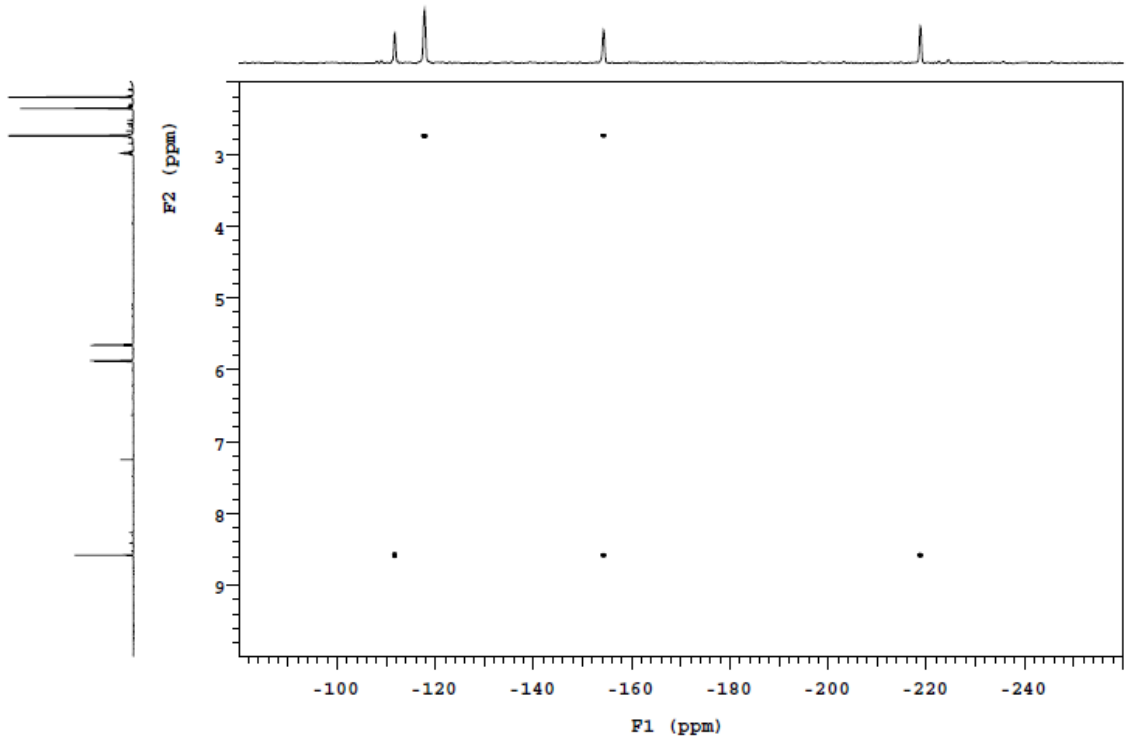

Fig. S8 ^{1}H-^{15}N HMBC spectrum recorded for the [(η^6-*p*-cym)Ru(tmtp)Cl_2] (**1**) in $CDCl_3$.

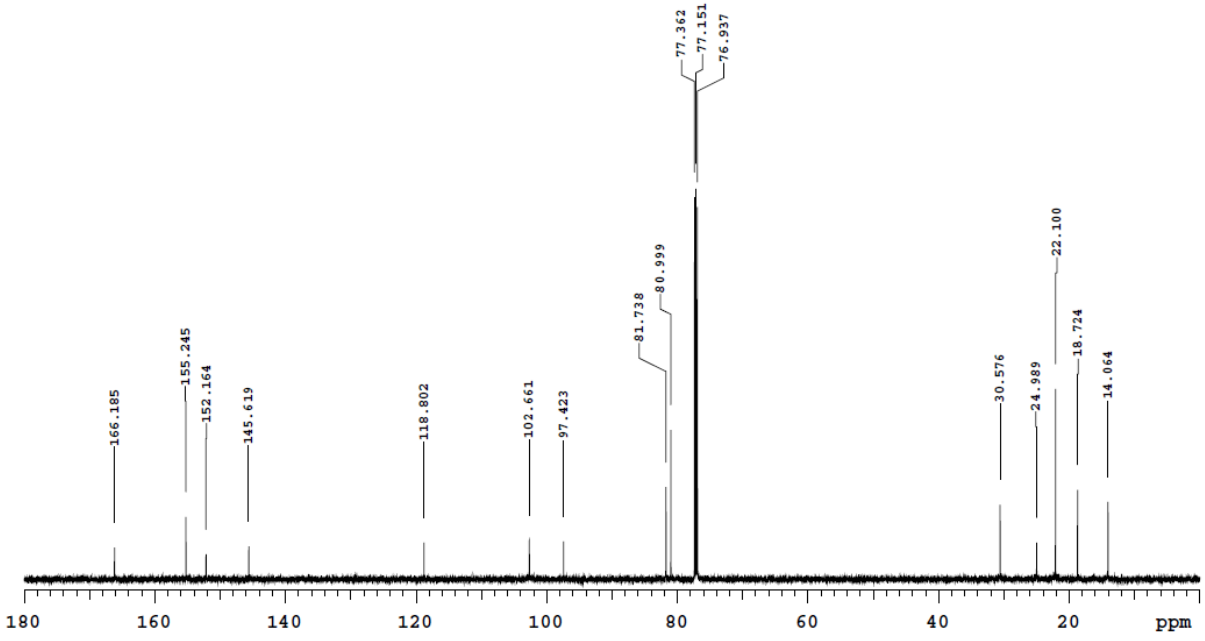

Fig. S9 ^{13}C NMR spectrum recorded for the [(η^6-*p*-cym)Ru(tmtp)Cl$_2$] (**1**) in CDCl$_3$.

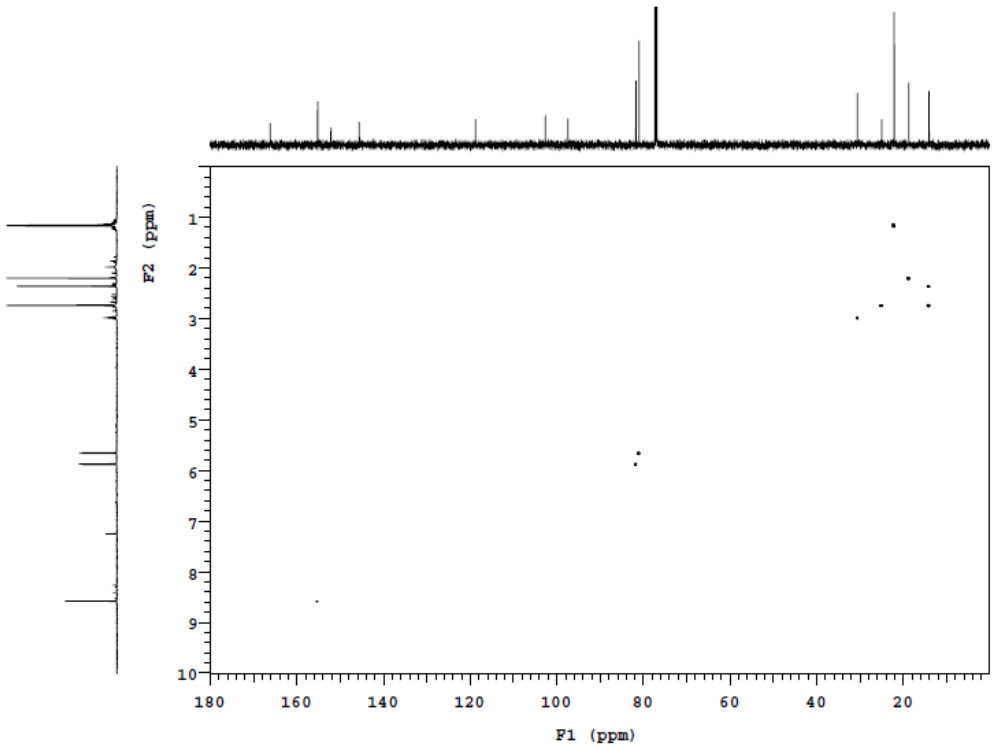

Fig. S10 ^{1}H-^{13}C HSQC spectrum recorded for the [(η^6-*p*-cym)Ru(tmtp)Cl$_2$] (**1**) in CDCl$_3$.

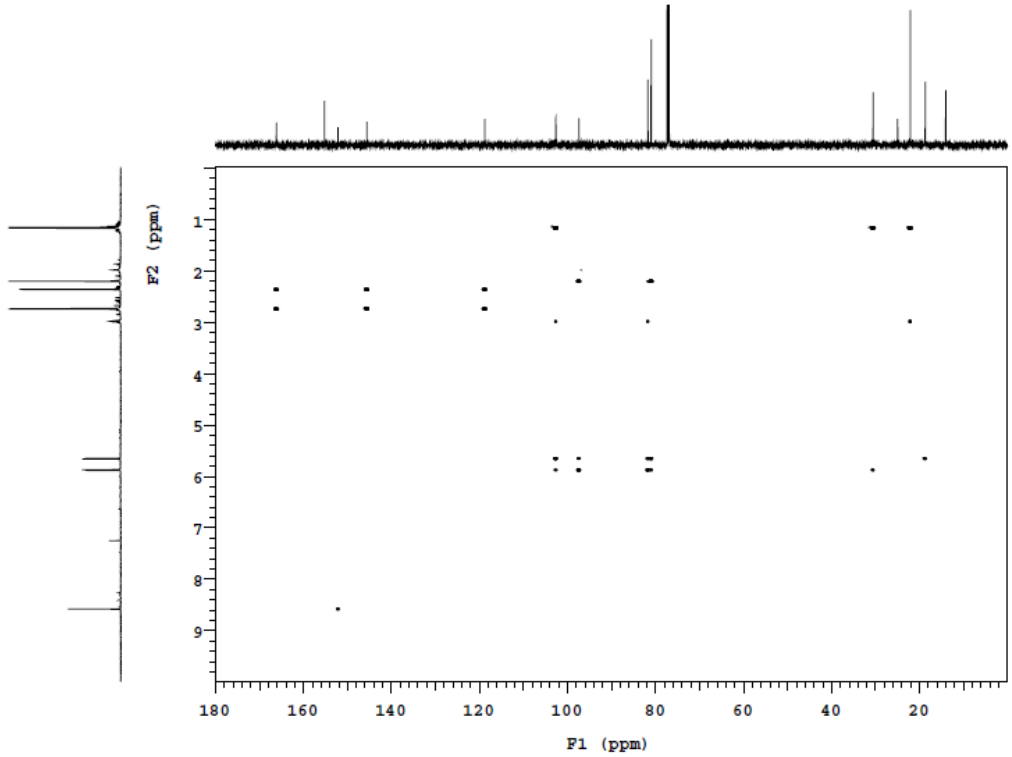

Fig. S11 ^{1}H-^{13}C HMBC spectrum recorded for the [(η^6-*p*-cym)Ru(tmtp)Cl_2] (**1**) in $CDCl_3$.

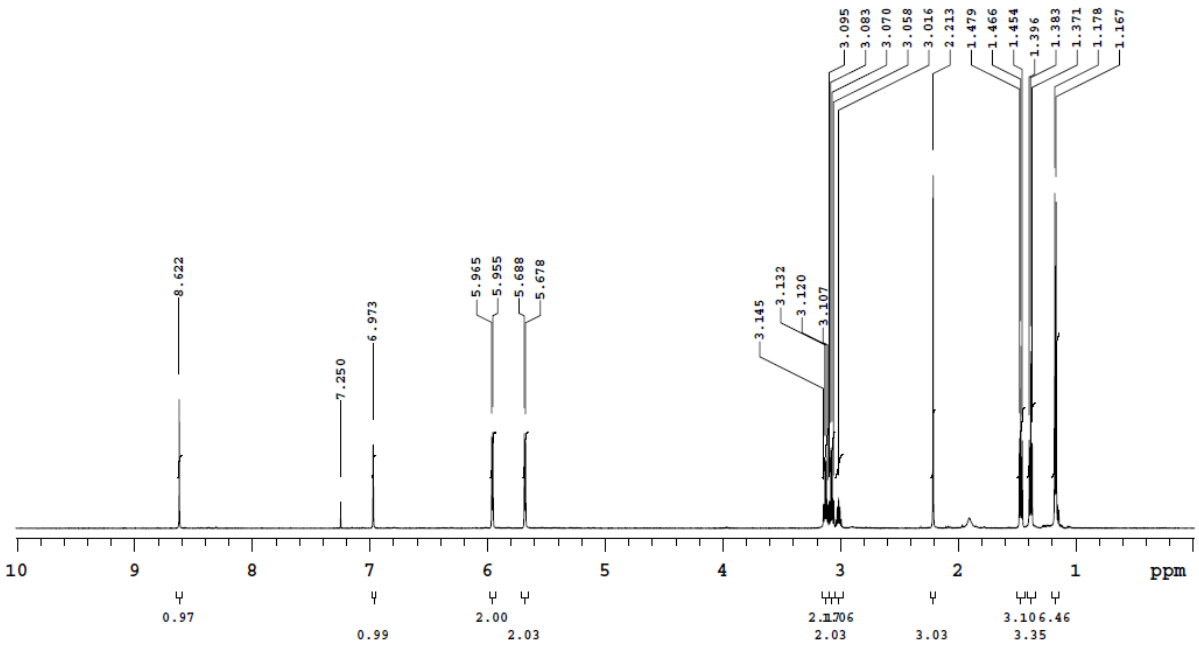

Fig. S12 ^{1}H NMR spectrum recorded for the [(η^6-*p*-cym)Ru(detp)Cl_2] (**2**) in $CDCl_3$.

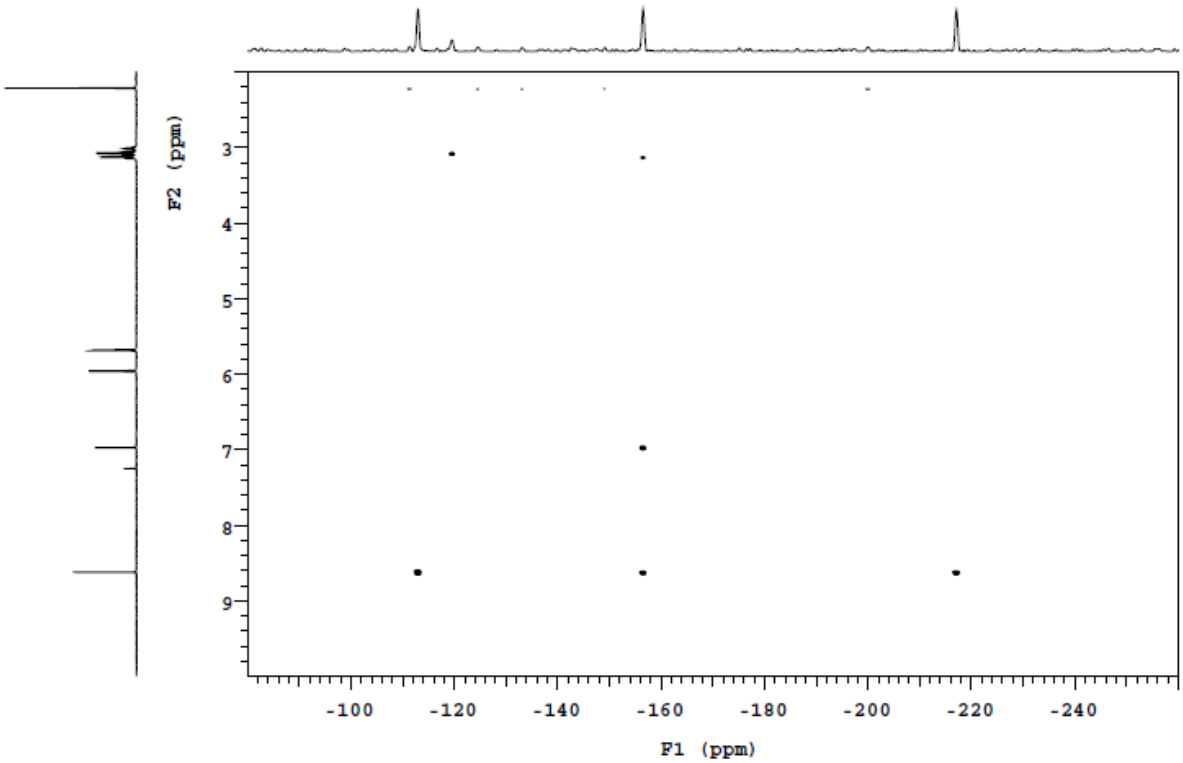

Fig. S13 ^{1}H-^{15}N HMBC spectrum recorded for the [(η^{6}-*p*-cym)Ru(detp)Cl$_2$] (**2**) in CDCl$_3$.

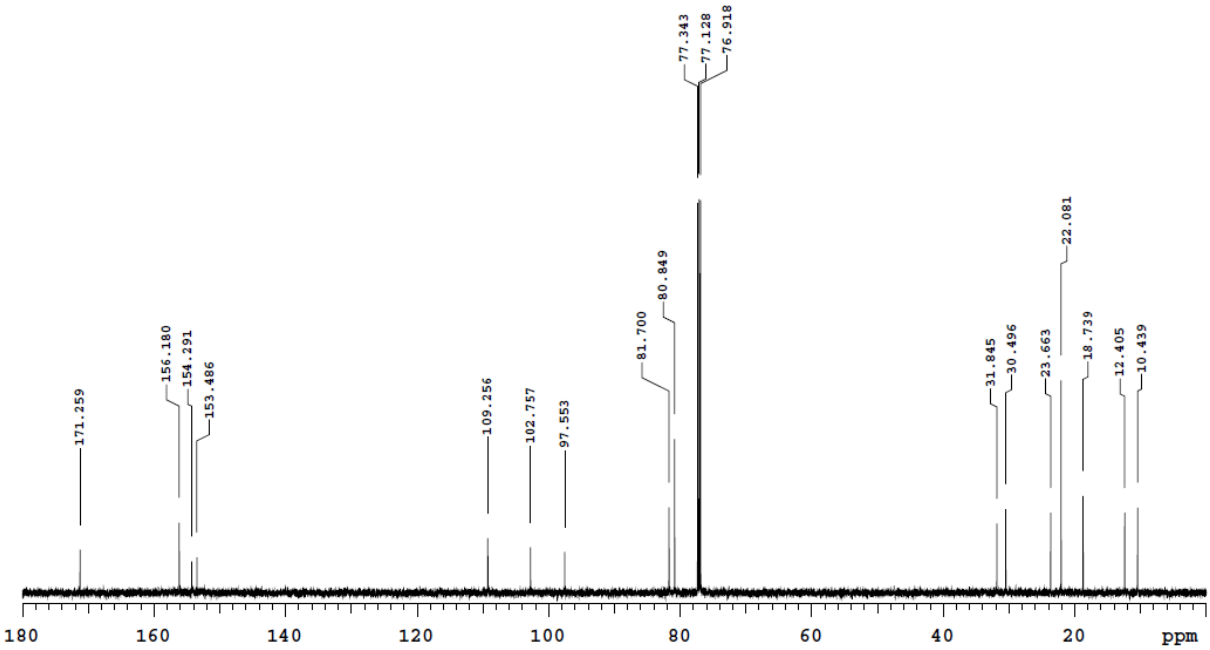

Fig. S14 ^{13}C NMR spectrum recorded for the [(η^{6}-*p*-cym)Ru(detp)Cl$_2$] (**2**) in CDCl$_3$.

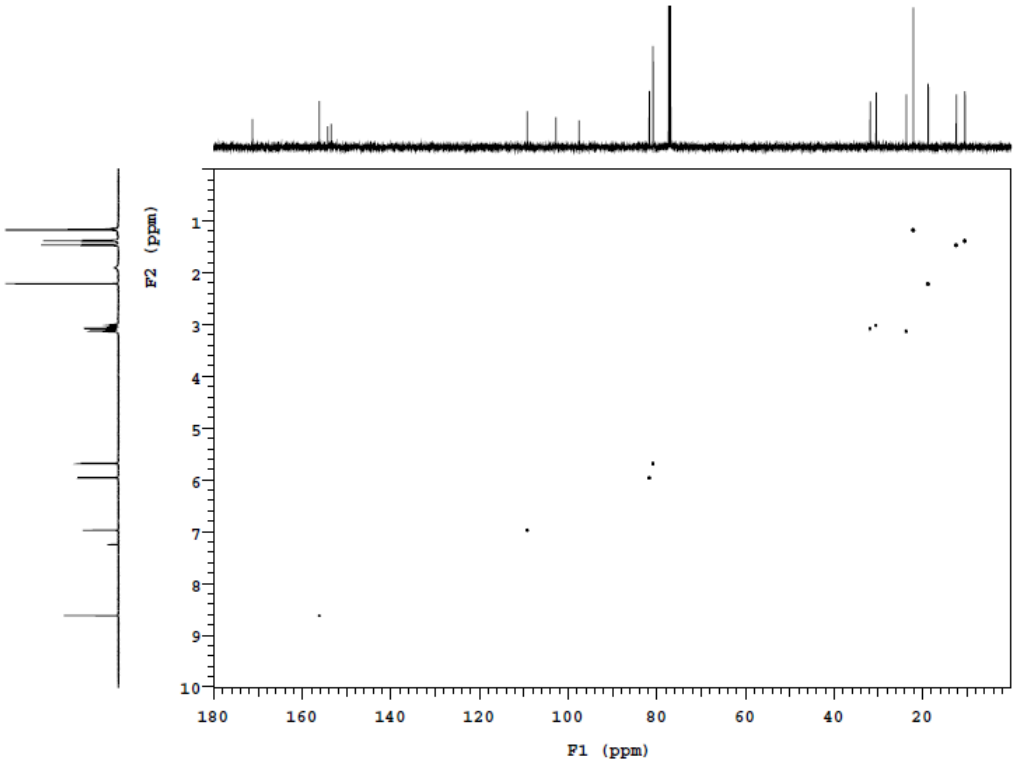

Fig. S15 ^{1}H-^{13}C HSQC spectrum recorded for the [(η^6-*p*-cym)Ru(detp)Cl_2] (**2**) in $CDCl_3$.

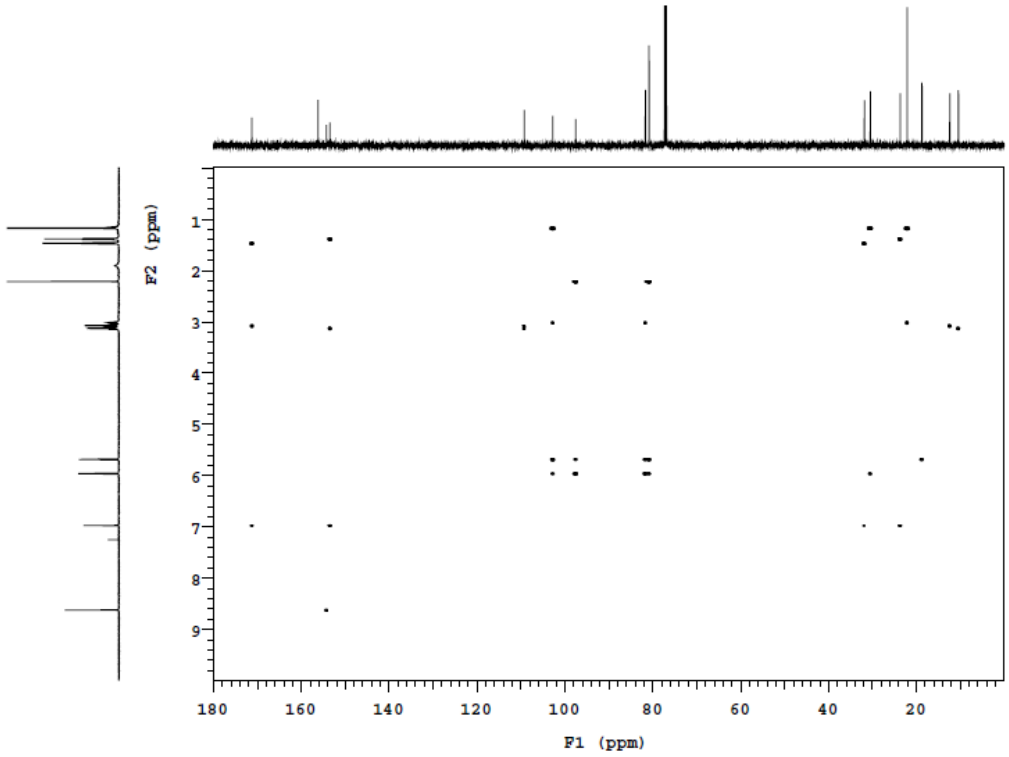

Fig. S16 ^{1}H-^{13}C HMBC spectrum recorded for the [(η^6-*p*-cym)Ru(detp)Cl_2] (**2**) in $CDCl_3$.

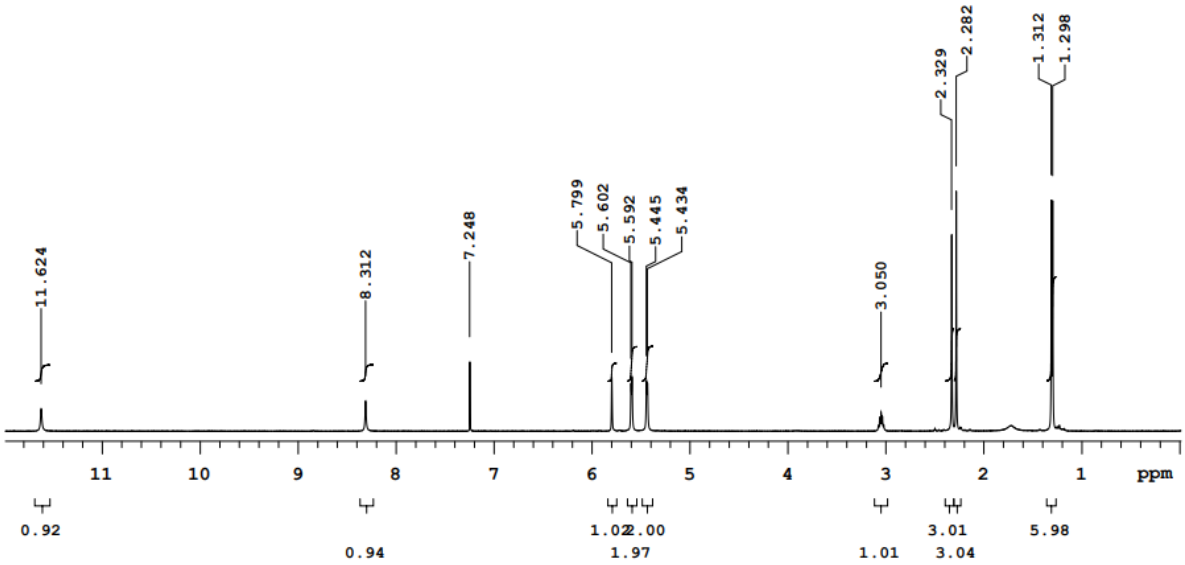

Fig. S17 ^{1}H NMR spectrum recorded for the [(η^6-*p*-cym)Ru(HmtpO)Cl_2] (**3**) in $CDCl_3$.

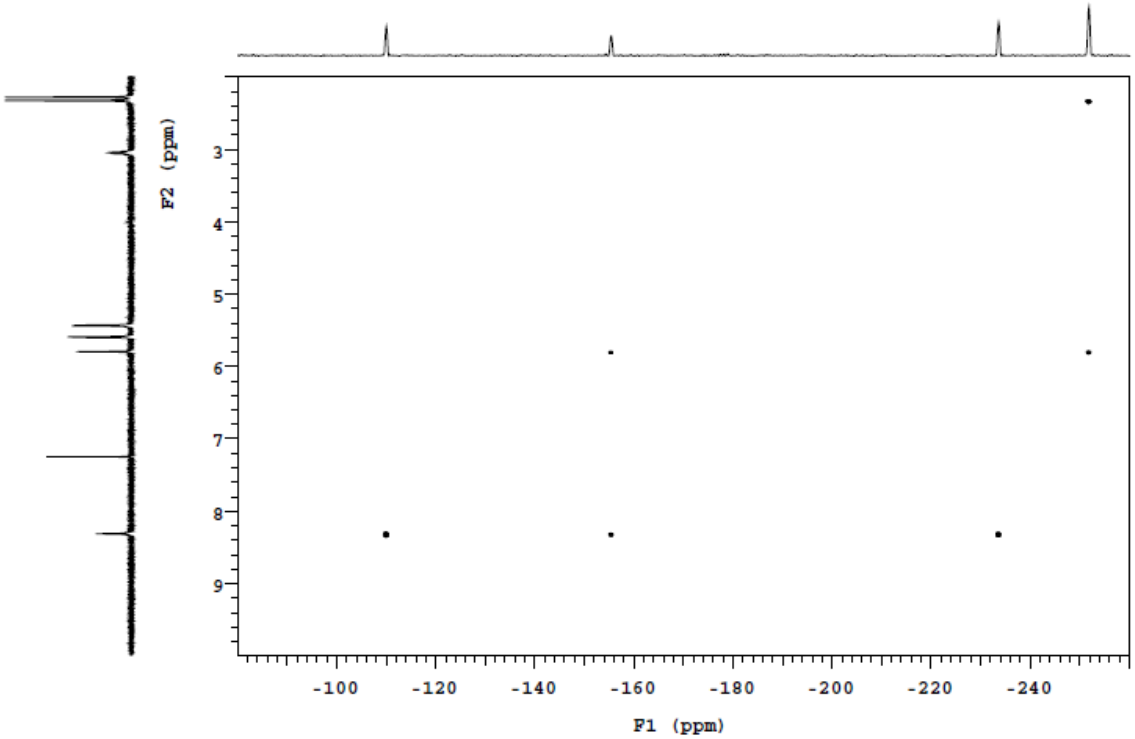

Fig. S18 ^{1}H-^{15}N HMBC spectrum recorded for the [(η^6-*p*-cym)Ru(HmtpO)Cl_2] (**3**) in $CDCl_3$.

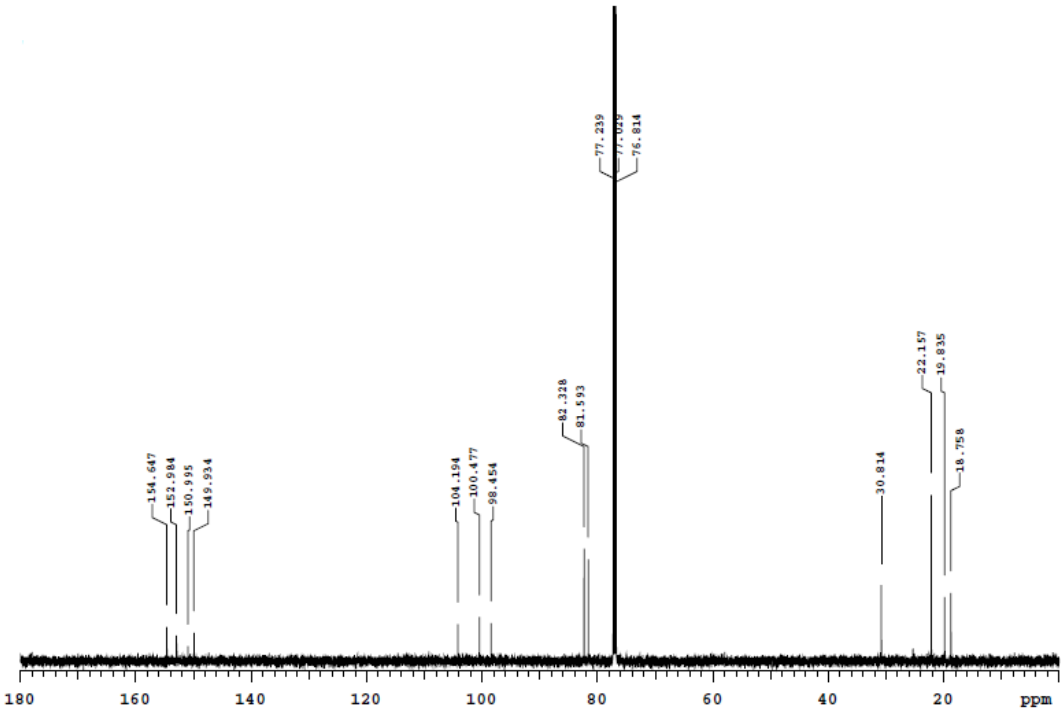

Fig. S19 ^{13}C NMR spectrum recorded for the [(η^6-*p*-cym)Ru(HmtpO)Cl$_2$] (**3**) in CDCl$_3$.

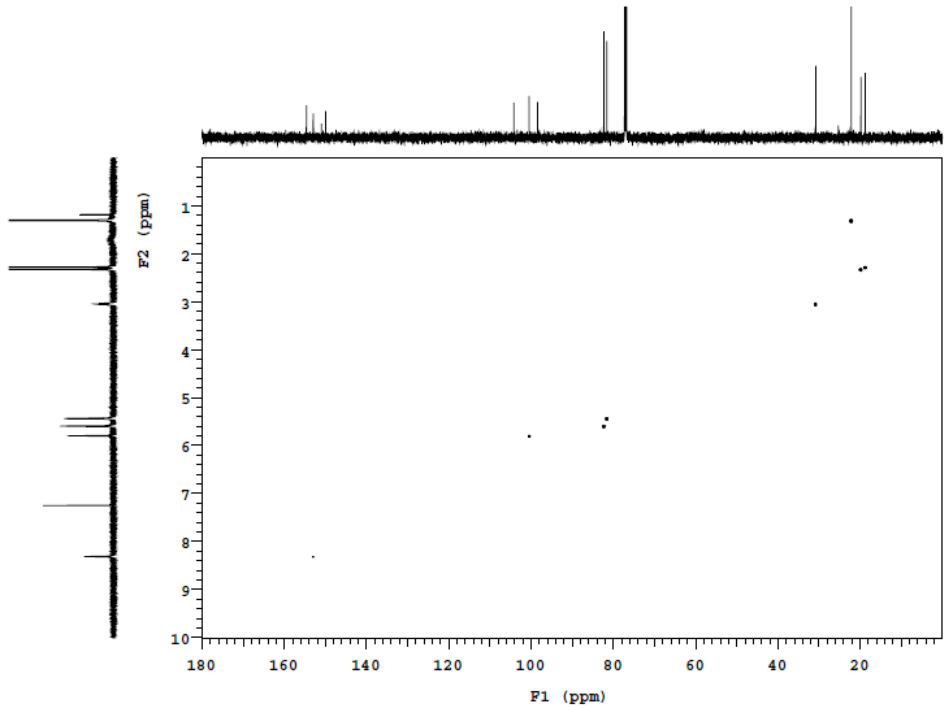

Fig. S20 ^{1}H-^{13}C HSQC spectrum recorded for the [(η^6-*p*-cym)Ru(HmtpO)Cl$_2$] (**3**) in CDCl$_3$.

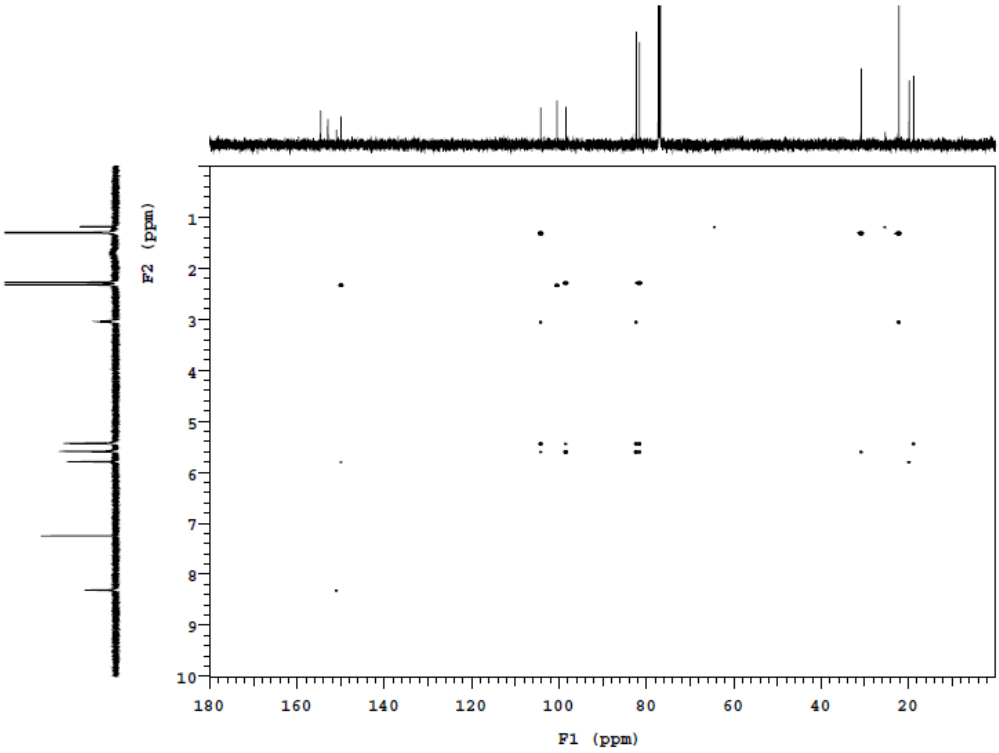

Fig. S21 ^{1}H-^{13}C HMBC spectrum recorded for the [(η^{6}-*p*-cym)Ru(HmtpO)Cl$_2$] (**3**) in CDCl$_3$.

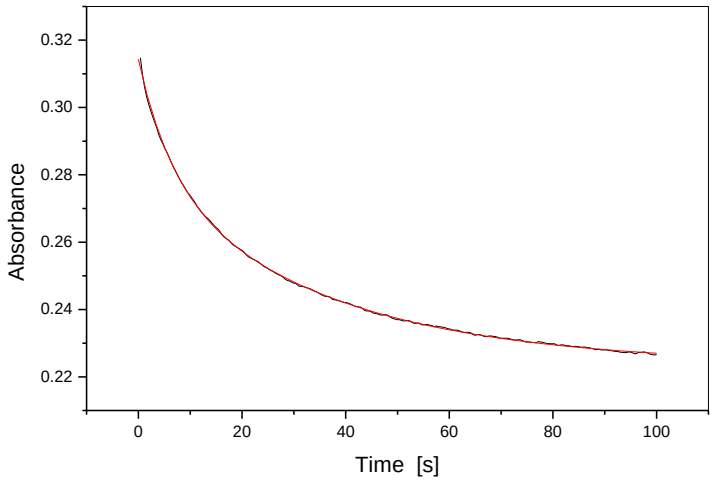

Fig. S22 Kinetic and fit trace for the base hydrolysis of the [(η^6-*p*-cym)Ru(tmtp)Cl_2] (**1**). Experimental conditions: [Ru^{II}] = 5 × 10^{-4} M, 100 mM phosphate buffer (OH^-, $H_2PO_4^-$, HPO_4^{2-}, PO_4^{3-}, Na^+), pH = 7, *T* = 298 K, t = 100 s, Δt = 0.02 s).

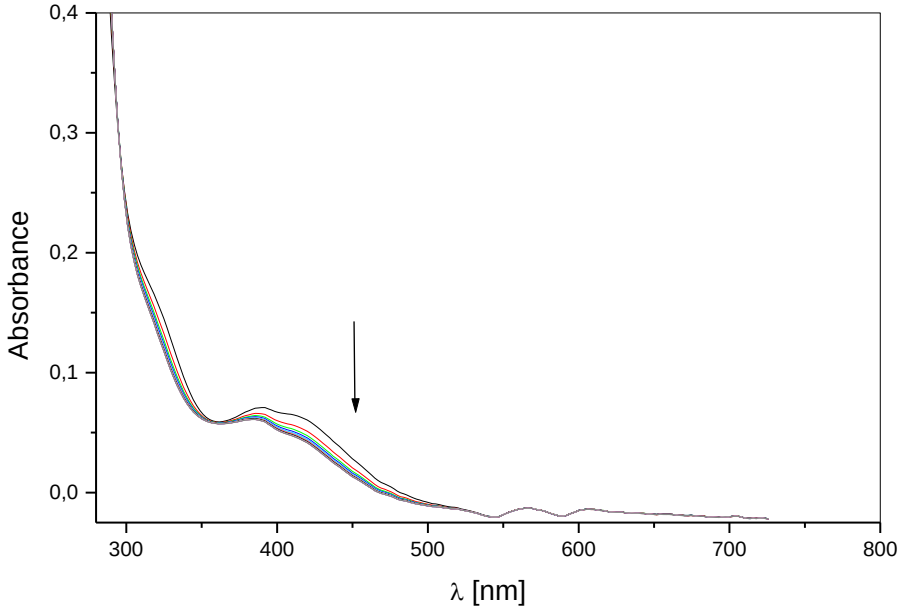

Fig. S23 Spectral changes observed during the base hydrolysis of the [(η^6-*p*-cym)Ru(detp)Cl_2] (**2**). Experimental conditions: [Ru^{II}] = 1 × 10^{-4} M, 100 mM phosphate buffer (OH^-, $H_2PO_4^-$, HPO_4^{2-}, PO_4^{3-}, Na^+), pH = 7, *T* = 298 K, t = 250 s, Δt = 12.5 s.

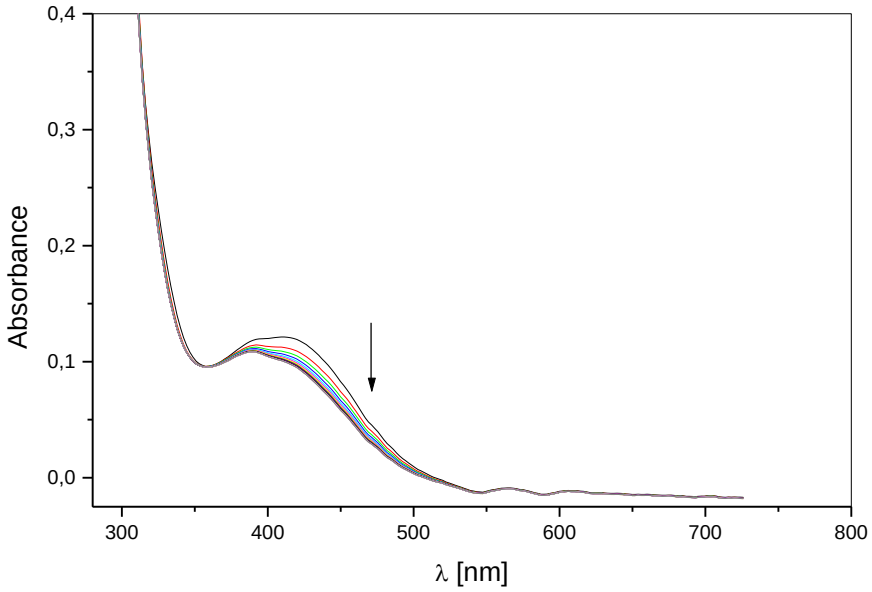

Fig. S24 Spectral changes observed during the base hydrolysis of the [(η^6-*p*-cym)Ru(HmtpO)Cl_2] (**3**). Experimental conditions: [Ru^{II}] = 2×10^{-4} M, 100 mM phosphate buffer (OH^-, $H_2PO_4^-$, HPO_4^{2-}, PO_4^{3-}, Na^+), pH = 7, *T* = 298 K, t = 250 s, Δt = 12.5 s.

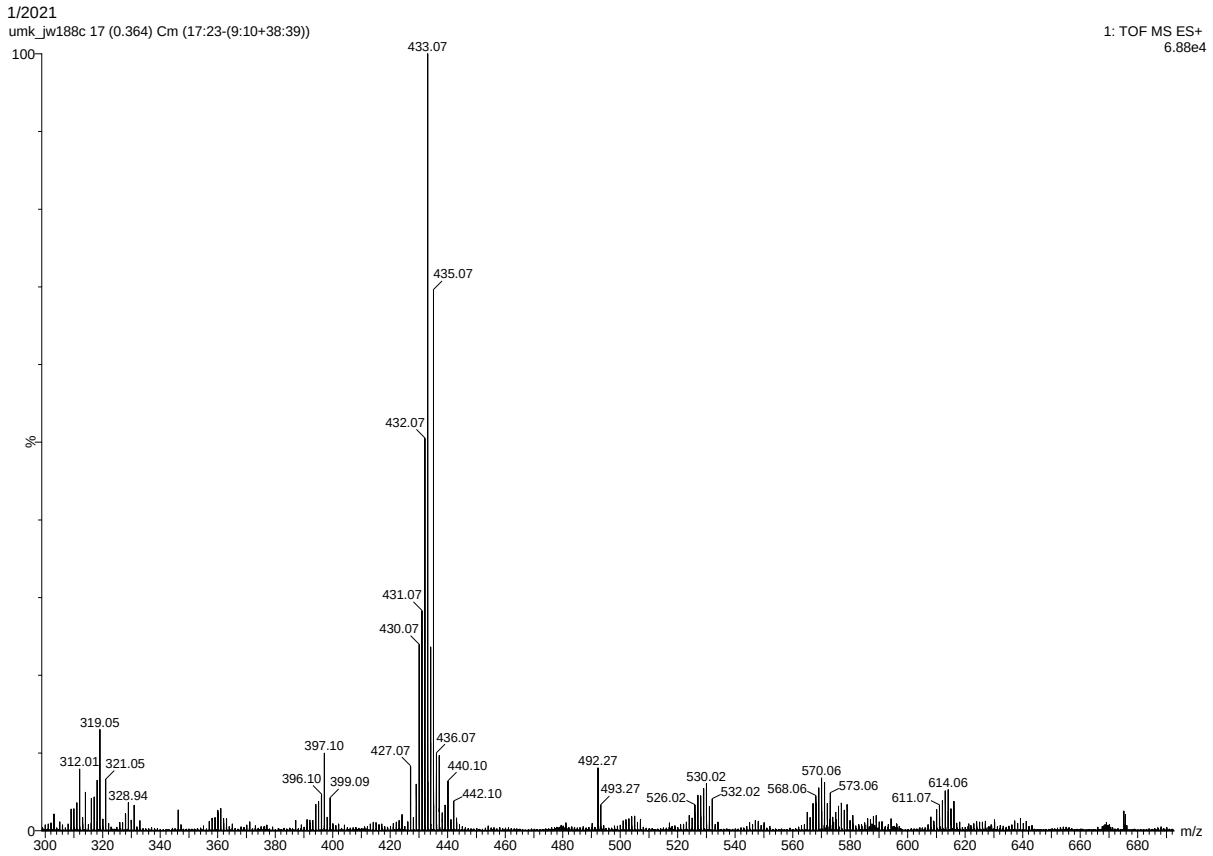

Fig. S25 Positive ion mode ESI-MS spectra of the [Ru(η^6-*p*-cym)(tmtp)Cl_2] (**1**) analysed directly after dissolving in ACN and mixing with H_2O.

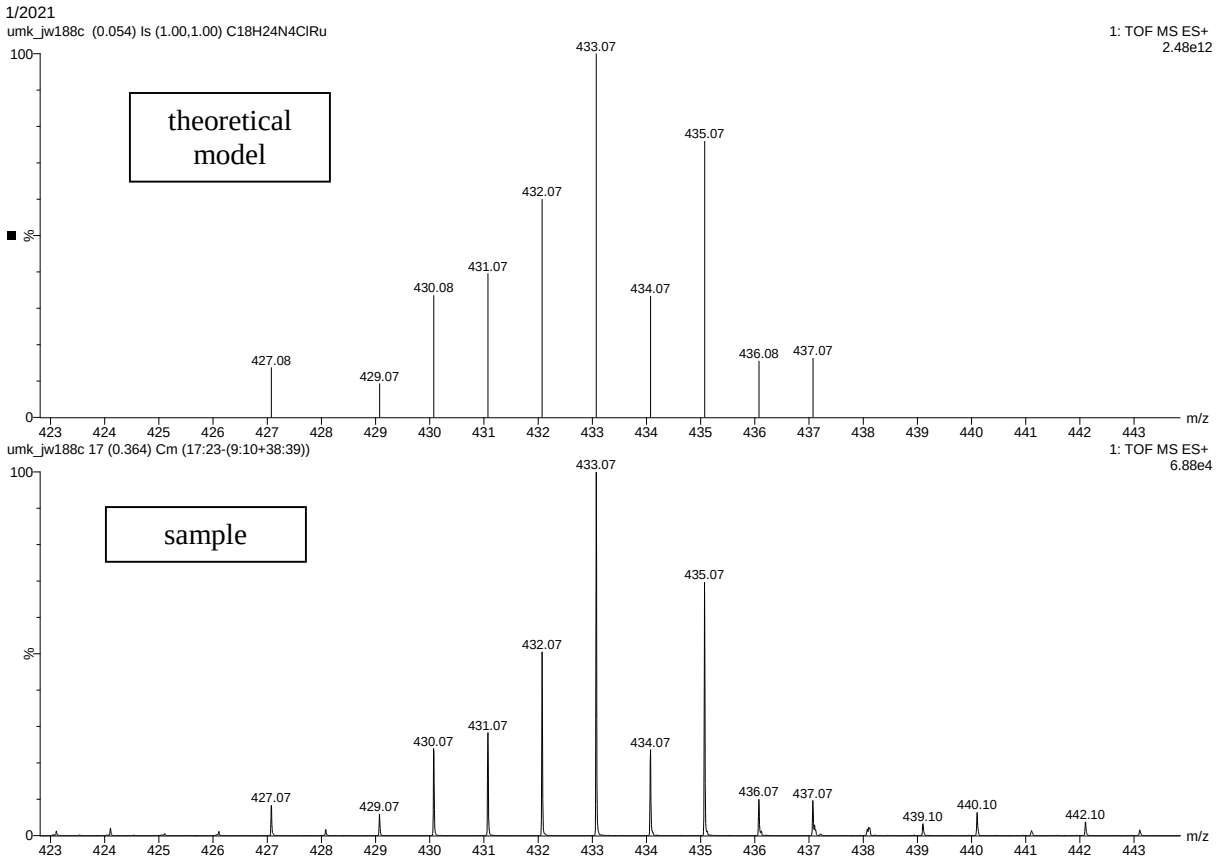

Fig. S26 The theoretical model of the signal at 433 m/z.

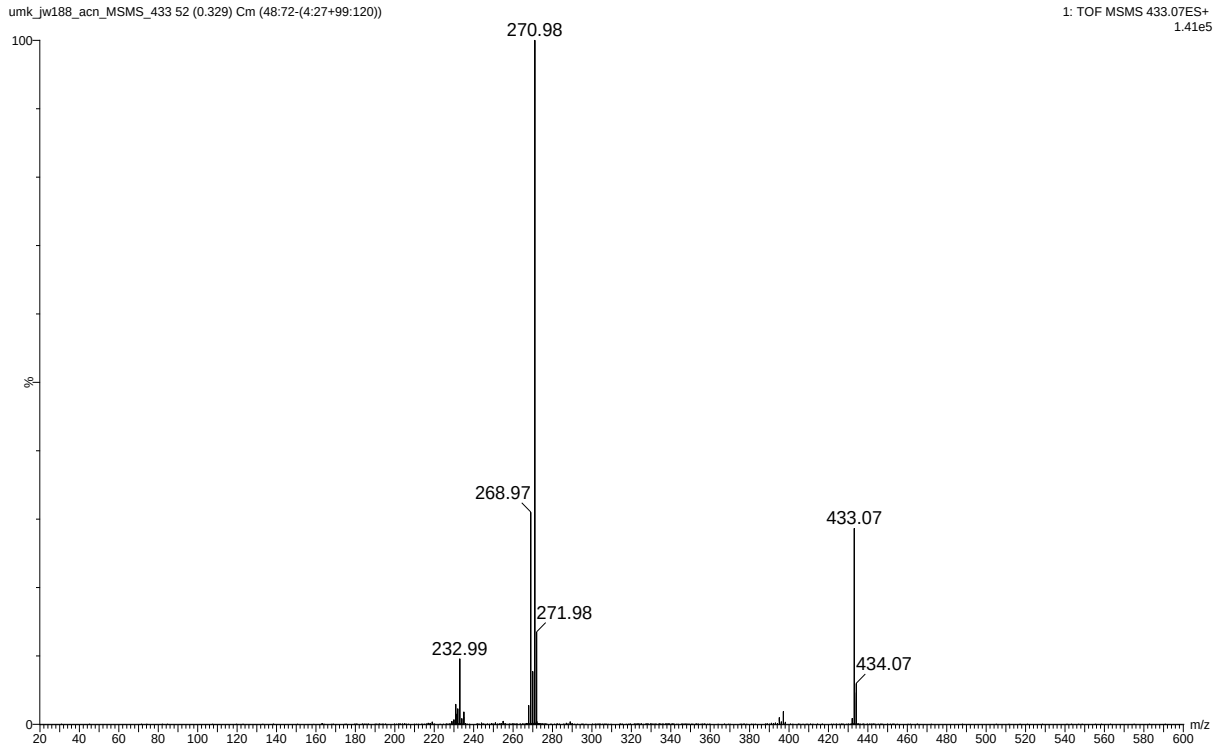

Fig. S27 Positive ion (ESI MS/MS) fragmentation spectra of the signal at 433 m/z.

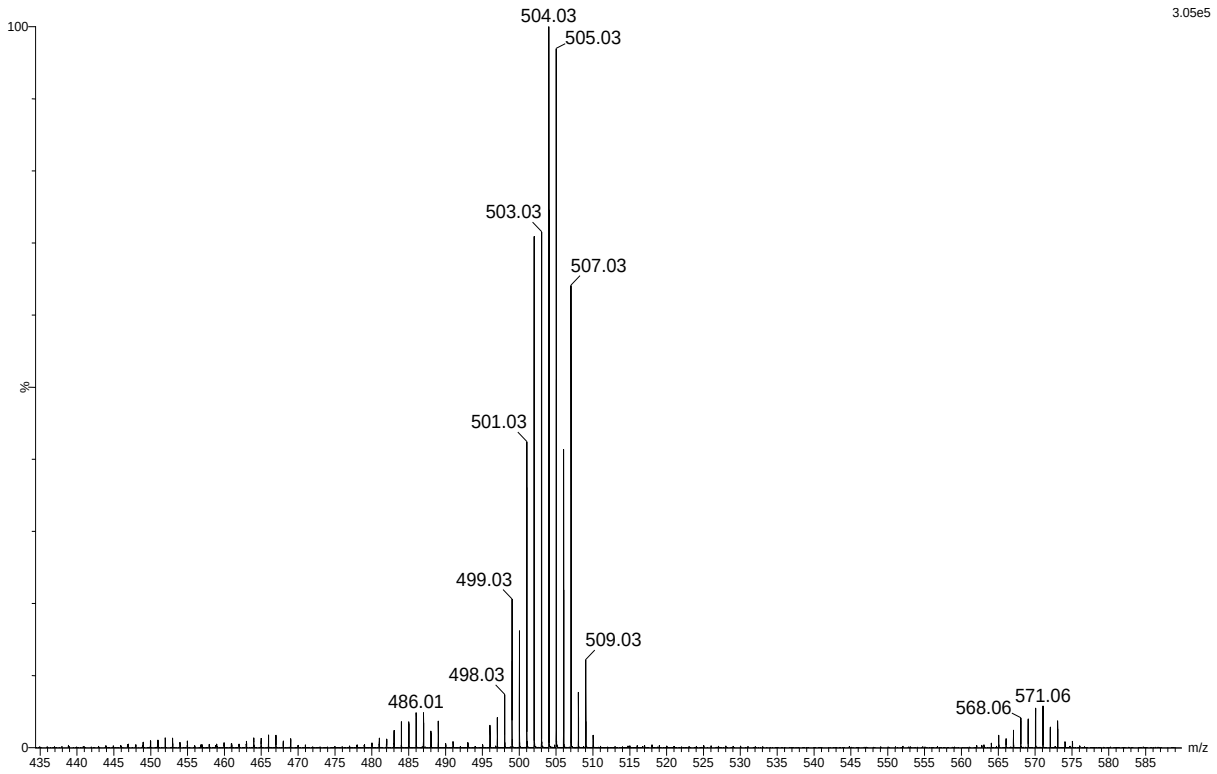

Fig. S28 Positive ion mode ESI-MS spectra of the fragment at 504 m/z after mixing with H_2O.

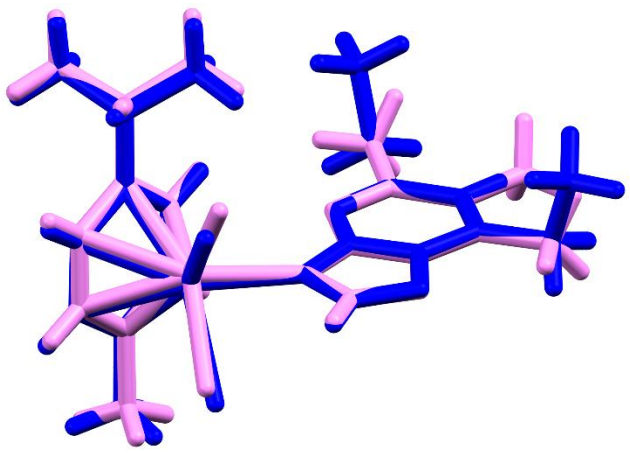

Fig. S29 Overlay of the molecular cores of **1** (pink) and **2** (blue).

Molecular packing

The differences in molecular packing are linked to the substituents on the triazolopyrymidine ring system, which in the case of **2** are much bigger and not positioned in the plane of the fused rings, with torsion angles N4-C5-C51-C52 = 82.6(3)°, C6-C5-C51-C52 = -94.4(3), C6-C7-C71-C72 = 95.9(4)°, and N8-C7-C71-C72 = -80.8(4)°. This causes the packing of the molecules to be slightly less dense, leading to the presence of minor voids in the crystal structure. PLATON calculates a potential solvent area volume of 23.4 $Å^3$ per unit cell (probe radius = 1.2 Å, grid = 0.20 Å), accounting for 2.3% of the total cell volume.[25] Weak hydrogen bonds, such as C-H---Cl, C-H---N and C-H---π, stabilise the packing arrangements in both complexes. Furthermore, π-π stacking of the triazolopyrimidines, with the interaction between the triazole of one and the pyrimidine ring of another bicycle; is observed in **2**, with a distance of 3.706(2) Å between their centroids. This type of interaction is not present in **1**.

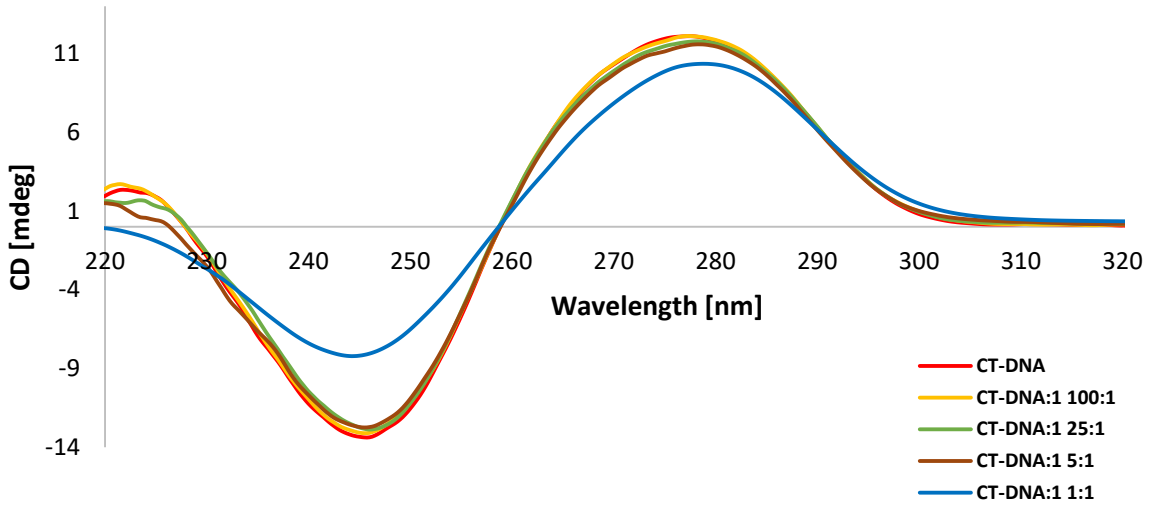

Fig. S30 CD spectra of CT-DNA (150 μM) after incubation for 24 h at 37 ºC with increasing concentrations of the [(η^6-*p*-cym)Ru(tmtp)Cl_2] (**1**) in 10 mM phosphate buffer (pH = 7.4).

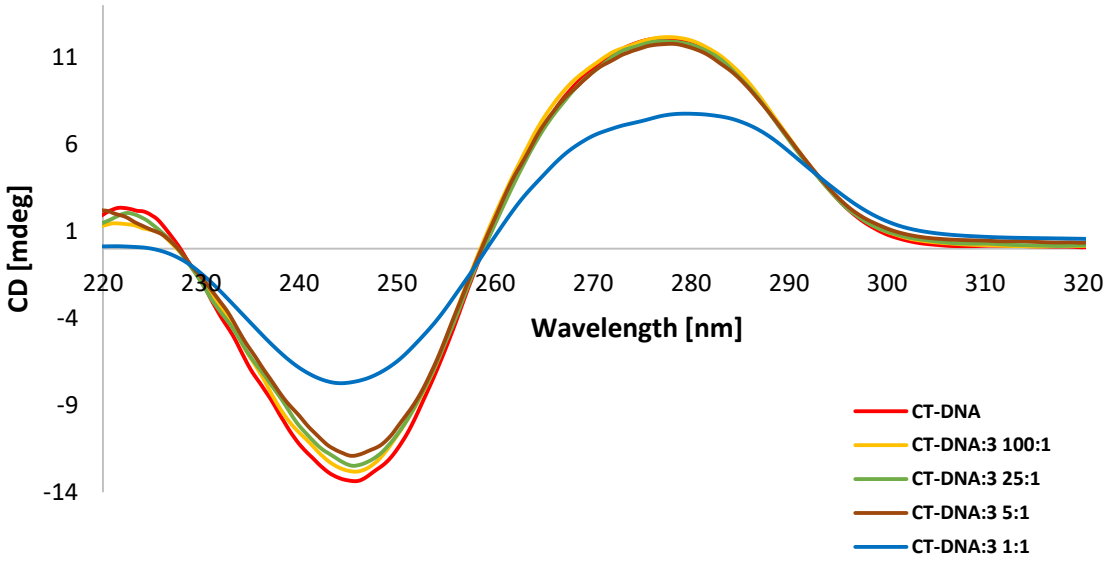

Fig. S31 CD spectra of CT-DNA (150 μM) after incubation for 24 h at 37 ºC with increasing concentrations of the [(η^6-*p*-cym)Ru(HmtpO)Cl_2] (**3**) in 10 mM phosphate buffer (pH = 7.4).

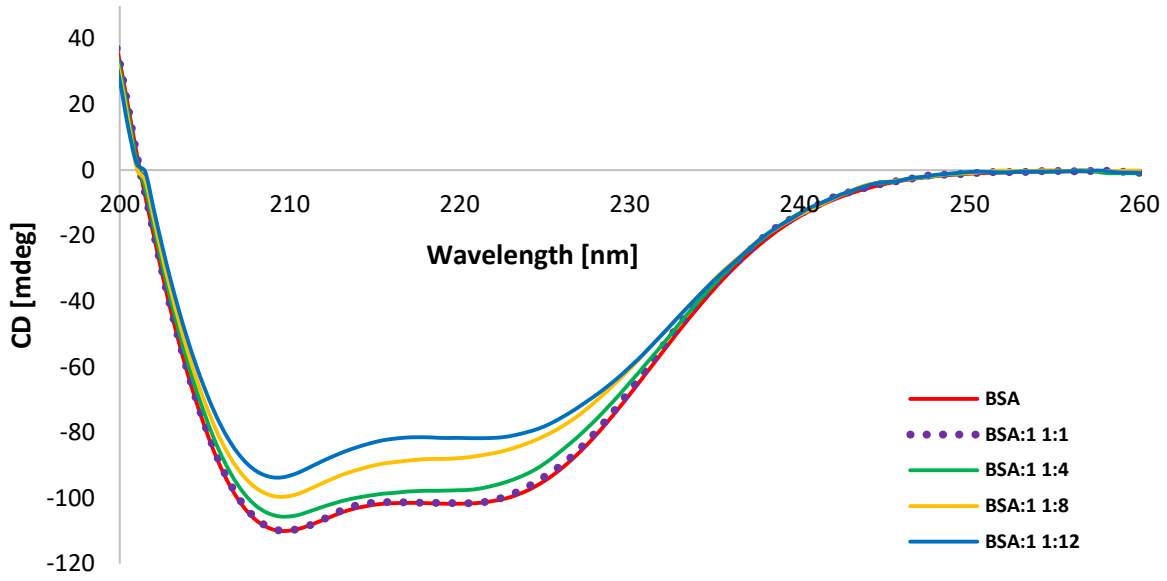

Fig. S32 CD spectra of BSA (1.5 μM) after incubation for 24 h at 37 °C with increasing concentrations of the [(η^6-*p*-cym)Ru(tmtp)Cl_2] (**1**) in 10 mM phosphate buffer (pH = 7.4).

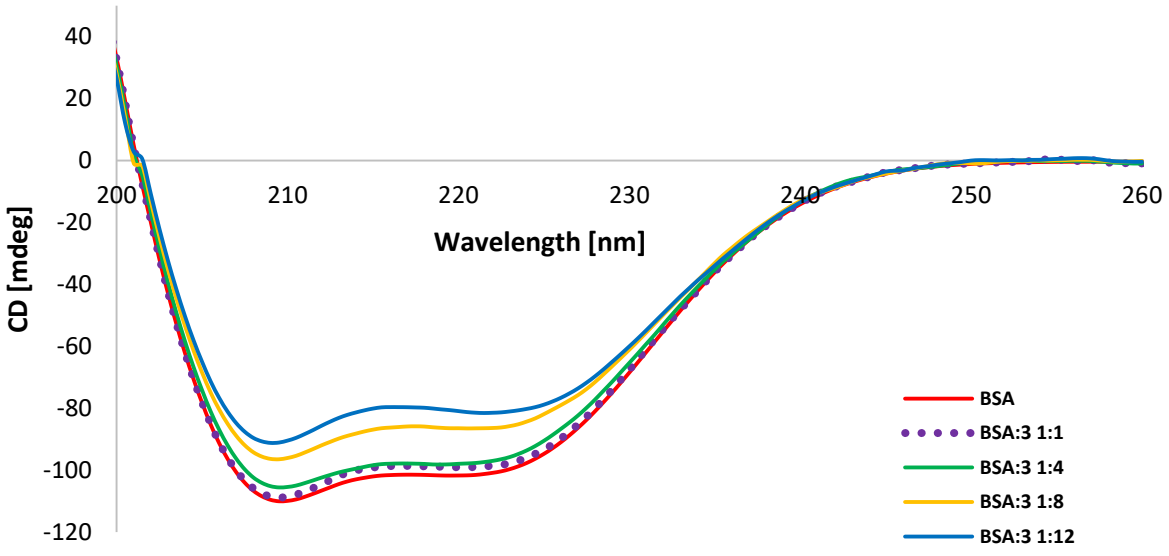

Fig. S33 CD spectra of CT-DNA (1.5 μM) after incubation for 24 h at 37 °C with increasing concentrations of the [(η^6-*p*-cym)Ru(HmtpO)Cl_2] (**3**) in 10 mM phosphate buffer (pH = 7.4).

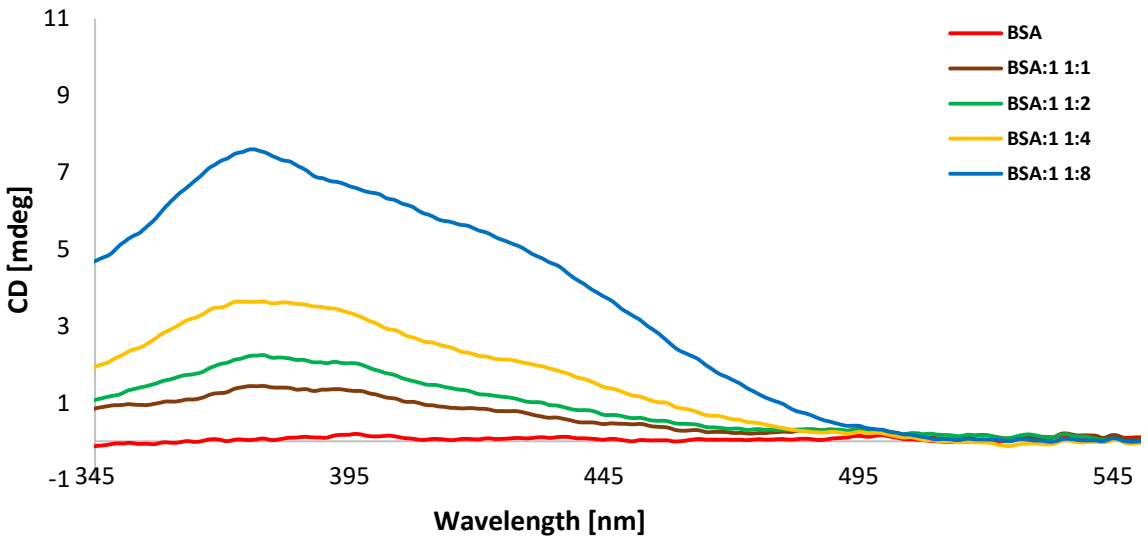

Fig. S34 CD spectra of CT-DNA (150 μM) after incubation for 24 h at 37 ºC with increasing concentrations of the [(η^6-*p*-cym)Ru(tmtp)Cl_2] (**1**) in 10 mM phosphate buffer (pH = 7.4).

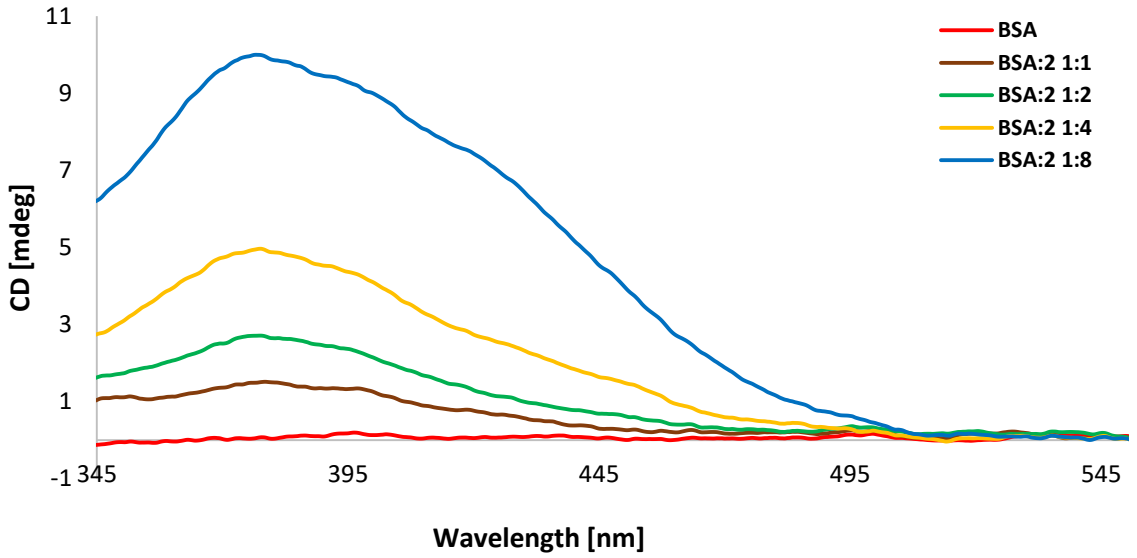

Fig. S35 CD spectra of CT-DNA (150 μM) after incubation for 24 h at 37 ºC with increasing concentrations of the [(η^6-*p*-cym)Ru(detp)Cl_2] (**2**) in 10 mM phosphate buffer (pH = 7.4).

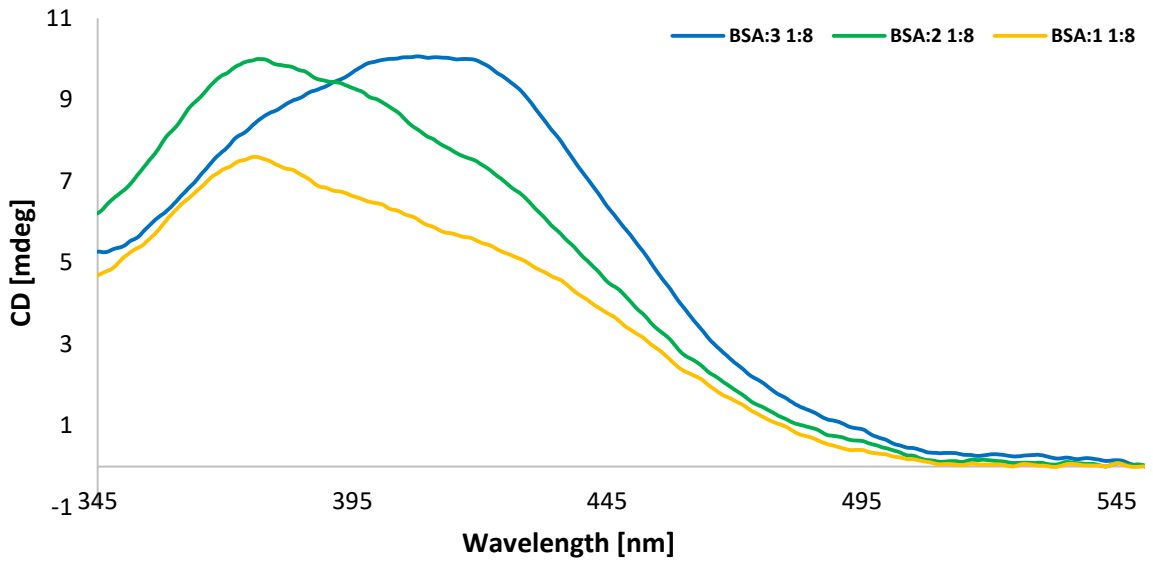

Fig. S36 Comparison of CD spectra of CT-DNA (150 μM) after incubation for 24 h at 37 ºC with **1**, **2** and **3** for 1:8 molar ratio (BSA:Ru complex) in 10 mM phosphate buffer (pH = 7.4).

References

[1] K. S. Neethu, J. Eswaran, M. Theetharappan, S. P. Bhuvanesh Nattamai, M. A. Neelakantan and K. M. Velusamy, *Appl. Organometal. Chem*., 2019, **33**, e4751.

[2] S. De, S. Ray Chaudhuri, A. Panda, G. Rahosaheb Jadhav, R. Selva Kumar, P. Manohar, N. Ramesh, A. Mondal, A. Moorthy, S. Banerjee, P. Paira and S. K. Ashok Kumar, *New J. Chem.*, 2019, **43**, 3291.

[3] F. Caruso, M. Rossi, A. Benson, C. Opazo, D. Freedman, E. Monti, M. Bruna Gariboldi, J. Shaulky, F. Marchetti, R. Pettinari and C. Pettinari, *J. Med. Chem.*, 2012, **55**, 1072.

[4] W. Guo, W. Zheng, Q. Luo, X. Li, Y. Zhao, S. Xiong and F. Wang, *Inorg. Chem.*, 2013, **52**, 5328.

[5] R. Prasad Paitandi, R. Shikha Singh, S. Mukhopadhyay, G. Sharma, B. Koch, P. Vishnoi and D. Shankar Pandey, *Inorg. Chim. Acta*, 2017, **454**, 117.

[6] R. Kumar Gupta, G. Sharma, R. Pandey, A. Kumar, B. Koch, P.-Z. Li, Q. Xu and D. Shankar Pandey, *Inorg. Chem.*, 2013, **52**, 13984.

[7] K. V. Miroshnychenko, A. V. Shestopalova, Molecular Docking of Biologically Active Substances to Double Helical Nucleic Acids: Problems and Solutions, Chapter 5 in S. Dastmalchi, M. Hamzeh-Mivehroud, B. Sokouti (Eds), Applied Case Studies and Solutions in Molecular Docking-Based Drug Design (Advances in Medical Technologies and Clinical Practice), IGI Global, USA, Hershey PA, 2016.

[8] W. K. Kasprzak, N. A. Ahmed and B. A. Shapiro, *Curr. Opin. Biotechnol*, 2020, **63**, 16.

[9] G. M. Morris, R. Huey and W. Lindstrom, *J. Comput. Chem.*, 2009, **30**, 2785.

[10] O. Trott, A and J. Olson, AutoDock Vina: improving the speed and accuracy of with a new scoring function, efficient optimization multithreading, *J. Comput. Chem.* 2010, **31**, 455.

[11] Discovery Studio 3.0; Accelrys, Inc.: 10188 Telesis Court, Suite 100, San Diego, CA 92121, USA.
[12] Sybyl X 1.1, Tripos, Inc.
[13] D. Mustard and D. W. Ritchie, *Proteins: Struct. Funct. Bioinf.*, 2005, **60**, 269.
[14] http://www.rcsb.org/ H. M. Berman, J. Westbrook, Z. Feng, G. Gilliland, T. N. Bhat, H. Weissig, I. N. Shindyalov and P. E. Bourne, The Protein Data Bank Nucleic Acids Research, 2000, **28**, 235.
[15] I. Petitpas, A. A. Bhattacharya, S. Twine, M. East and S. Curry, *J. Biol. Chem.*, 2001, **276**, 22804.
[16] G.-Y. Chuang, D. Kozakov, R. Brenke, S. R. Comeau and S. Vajda, *Biophysical Journal*, 2008, **95**, 4217.
[17] G. Jones, P. Willett, R. C. Glen, A. R. Leach and R. Taylor, *J. Mol. Biol.*, 1997, **267**, 727.
[18] Y. Li, L. Han, Z. Liu and R. Wang, *J. Chem. Inf. Model.*, 2014, **54**, 1717.
[19] P. Paneth and A. Paneth, Docking scores to SARS-CoV-2 S-protein, human ACE2 receptor and their interface from ChemPLP docking algorithm as implemented in the Gold program, unpublished results available at figshare https://doi.org/10.6084/m9.figshare.12130932.v1
[20] J.-D. Chai and M. Head-Gordon, *J. Chem. Phys.*, 2008, **128**, 084106.
[21] J.-D. Chai and M. Head-Gordon, *Phys. Chem. Chem. Phys.*, 2008, **10**, 6615.
[22] F. Weigend and R. Ahlrichs, *Phys. Chem. Chem. Phys.*, 2005, **7**, 3297.
[23] M. J. Frisch, G. W. Trucks, H. B. Schlegel et al. Gaussian, Version 16, Gaussian, Inc.: Wallingford, CT, USA, 2016.
[24] C. A. Grambow, L. Pattanaik and W. H. Green, *Sci. Data*, 2020, **7**, 137.
[25] A. L. Spek, *Acta Cryst.*, D65, 2009, 148.